Abstract

The linear analysis of turbomachinery aeroelasticity is based on the linearization of the unsteady flow equations around the mean flow field which can be determined by a nonlinear steady solver. The unsteady periodic flow can be decomposed into a sum of harmonics, each of which can be computed independently solving a set of linearized equations. The analysis considers just one particular frequency of unsteadiness at a time and the objective is to compute a complex flow solution which represents the amplitude and phase of the unsteady flow. The solution procedure of both the nonlinear steady and the linear harmonic Euler/Navier-Stokes solvers of the $HYDRA$ suite of codes consists of a preconditioned fixed-point iteration. This paper documents the numerical instabilities encountered solving the linear harmonic equations for some turbomachinery test cases, highlights their physical origin and summarizes the implementation of a GMRES algorithm aiming at the stabilization of the linear code. Presented results include the flutter analysis of a two-dimensional turbine section and a civil engine fan.

1

Effects of Flow Instabilities on the Linear Analysis of Turbomachinery Aeroelasticity

M.Sergio Campobasso [*]   and   Michael B. Giles [†]

Oxford University Computing Laboratory

Oxford, UK

March 27, 2003

[*]Research Officer, OUCL, Parks Road, OX1 3QD Oxford, UK

[†]Professor of Computational Fluid Dynamics, OUCL, Parks Road, OX1 3QD Oxford, UK

1 Introduction

The aeroelastic phenomena of concern in the turbomachinery industry are blade
flutter and forced response, as they may both lead to dramatic mechanical failures if
not properly accounted for in the design of the engine. The blades of an assembly
can undergo flutter vibrations when the aerodynamic damping associated with
certain flow regimes becomes negative and is not counterbalanced by the mechanical
damping. In such circumstances, the free vibration of the blades triggered by any
temporary perturbation is sustained through the energy fed into the structure by
the unsteady aerodynamic forces. The *high cycle fatigue* (HCF) caused by these
vibrations may shorten the life of the blades below the target life of the engine.
Blade forced response may also lead to HCF and is caused by the relative motion
of adjacent frames of reference, which transforms steady circumferential variations
of the flow field in one frame into periodic time-varying forces acting on the blades
in the other. Well known examples include forcing due to the wakes shed by an
upstream blade-row and fan inlet distortions due to cross-wind conditions.

The unsteady aerodynamic analysis intended for turbomachinery aeroelastic
predictions must be applicable over wide ranges of blade-row geometries and op-
erating conditions as well as unsteady excitation modes and frequencies. Also,
because of the large number of controlling parameters involved, there is a stringent
requirement for computational efficiency. Over the past two decades, a number of
approaches have emerged to carry out the analysis of turbomachinery aeroacous-
tics and aeroelasticity [1]. These methods vary from uncoupled linearized poten-
tial flow solvers in which the structural equations are solved independently of the
aerodynamics [2, 3] to fully-coupled nonlinear three-dimensional unsteady viscous

methods in which the structural and aerodynamic time-dependent equations are solved simultaneously [4]. Within this range, the uncoupled linear harmonic Euler and Navier-Stokes (NS) methods have proved to be a successful compromise between accuracy and cost and are now widely preferred in industry as a fast and accurate tool for aeroelastic predictions. Indeed, a growing body of evidence indicates that linear viscous calculations are adequate for a surprisingly large range of applications [5, 6, 7, 8]. This method views the aerodynamic unsteadiness as a small perturbation of the space-periodic mean steady flow. Hence the unsteady flow field can be linearized about it and due to linearity can be decomposed into a sum of harmonic terms, each of which can be computed independently. The cyclic periodicity of both the steady and unsteady flow leads to a great reduction of computational costs, since the analysis can focus on one blade passage rather than the whole blade-row making use of suitable periodic boundary conditions. The small amplitude of the aerodynamic unsteadiness often allows one to neglect both the coupling and variations of structural eigenmodes due to the aerodynamic forces [9]. Therefore the investigation can be carried out considering one structural mode at a time, determined by a finite-element program and used as an input for calculating the unsteady aerodynamic forces. The complete aerodynamic analysis consists of two phases: *a*) calculation of the nonlinear steady flow field about which the linearization is performed and *b*) solution of the linear harmonic equations.

The *HYDRA* suite of parallel codes [10, 11, 12] includes both a nonlinear (*hyd*) and a linear harmonic (*hydlin*) NS solver. The solution procedure for both *hyd* and *hydlin* can be viewed as a preconditioned fixed-point iteration. Usually the linear code converges without difficulty, but problems have been encountered

in situations in which the steady flow calculation itself failed to converge to a steady state but instead finished in a low-level limit cycle, often related to some physical phenomenon such as vortex shedding at a blunt trailing edge, unsteady shock/boundary layer or shock/wake interaction. The main objectives of this paper are to

- highlight and discuss the relationship between the numerical instabilities of the linear solver for some turbomachinery test cases and the physical properties of the underlying base flow;

- demonstrate the effectiveness of the *Generalized Minimum Residuals* (GMRES) algorithm [13] for retrieving the numerical stability of the linear code.

Sections 2 and 3 present an overview of the steady nonlinear and unsteady linear model respectively; the main features of the GMRES solver and some basic concepts concerning the numerical stability of fixed-point iterations are provided in section 4. Finally, section 5 presents two realistic applications, the flutter analysis of a two-dimensional turbine section for subsonic and transonic working conditions and that of a civil engine fan from near-choke to near-stall operating conditions.

2   Nonlinear flow analysis

The time-dependent Euler and Reynolds-averaged NS equations in conservative form are approximated on unstructured hybrid grids, using an edge-based discretization [14]. Considering the computational domain consisting of all the passages of a blade-row leads to a system of nonlinear ordinary differential equations

5

$(ODE's)$ of the form:

$$T\,\frac{d\mathbf{U}}{dt} + \mathbf{R}(\mathbf{U},\mathbf{U}_b,\mathbf{X},\dot{\mathbf{X}}) = 0 \,, \tag{1}$$

where t is the physical time, T is the Jacobian of the transformation from primitive to conservative variables, $\mathbf{U}$ is the vector of primitive flow variables, $\mathbf{R}$ is the nodal residual, $\mathbf{X}$ and $\dot{\mathbf{X}}$ are the vectors of nodal coordinates and velocities respectively. The vector $\mathbf{U_b}$ is used to enforce time-dependent disturbances at the inflow and outflow boundaries such as wakes shed by an upstream blade row. Each edge of the grid contributes only to the residuals corresponding to the two nodes at either end and the residual vector $\mathbf{R}$ depends also on the nodal velocities $\dot{\mathbf{X}}$, because the grid can deform following the blade vibration. The system (1) has size $(N_{eqs} \times N_0)$, where N_0 is the number of grid nodes, $N_{eqs} = 5$ for the inviscid flow model and $N_{eqs} = 6$ for turbulent flows. The 6th component in the latter case is the turbulence variable, determined with the Spalart-Almaras turbulence model. The residuals $\mathbf{R}$ also include the source terms due to the centrifugal and Coriolis forces, since the equations refer to the relative frame of reference.

The first stage of the aeroelastic analysis requires the computation of the mean steady flow $\overline{\mathbf{U}}$ about which the linearization of the unsteady terms will be carried out. Neglecting the time-dependent terms in the governing equations (1) and denoting by $\overline{\mathbf{X}}$ the mean nodal coordinates yields

$$\mathbf{R}(\overline{\mathbf{U}},\overline{\mathbf{X}}) = 0 \,, \tag{2}$$

which can be solved for a single blade-passage, as the mean flow is circumferentially periodic. The system (2) has size $(N \times N_{eqs})$ where $N = N_0/N_{blades}$ and N_{blades} is the number of blades in the blade-row. The boundary conditions to which the

system (2) is subject can be of three types: inflow/outflow, periodic and inviscid/viscous wall. The inflow and outflow boundaries are handled through fluxes which incorporate prescribed flow information and thus they become part of the residual vector $\mathbf{R}$. At matching pairs of periodic nodes the periodicity condition for linear cascades is enforced setting the flow state on the upper boundary equal to that on its lower counterpart. In the case of annular domains because of the use of Cartesian coordinates, the velocity vectors on the upper boundary are obtained by rotating those on the lower one. Combining flux residuals at the two periodic nodes in a suitable manner to maintain periodicity, this boundary condition can also be included in the definition of the flux residual vector $\mathbf{R}$.

A no-slip boundary condition is applied to viscous walls discarding the momentum residuals and replacing these equations by the specification of zero velocity at the boundary nodes. The computation of the flux residuals at nodes on inviscid walls is based on zero mass flux through the boundary faces, but in addition flow tangency is enforced by setting the normal component of the surface velocity to zero and disregarding the normal component of the momentum residuals. Applying these *strong wall boundary conditions* [15] to the system (2) yields:

$$
\begin{aligned}
(I - B)\, \mathbf{R}(\overline{\mathbf{U}}, \overline{\mathbf{X}}) &= 0 \\
B\, \overline{\mathbf{U}} &= 0\,,
\end{aligned}
\tag{3}
$$

where B is a projection matrix which extracts the momentum/velocity components at the wall boundaries. The discrete equations (3) are solved using Runge-Kutta time-marching accelerated by Jacobi preconditioning and multigrid [14].

3   Linear unsteady flow analysis

Due to the small level of unsteadiness, the time-dependent variables can be written
as the sum of a mean steady part and a small amplitude perturbation:

$$\mathbf{X}(t) = \overline{\mathbf{X}} + \tilde{\mathbf{x}}(t), \qquad ||\tilde{\mathbf{x}}|| \ll ||\overline{\mathbf{X}}||$$

$$\mathbf{U}_b(t) = \overline{\mathbf{U}}_b + \tilde{\mathbf{u}_b}(t), \qquad ||\tilde{\mathbf{u}_b}|| \ll ||\overline{\mathbf{U}}_b||$$

$$\mathbf{U}(t) = \overline{\mathbf{U}} + \tilde{\mathbf{u}}(t), \qquad ||\tilde{\mathbf{u}}|| \ll ||\overline{\mathbf{U}}|| \,,$$

where the perturbations are overlined with a *tilde* symbol. Linearizing equations
(1) about the mean steady conditions $(\overline{\mathbf{X}}, \overline{\mathbf{U}})$ yields

$$T\frac{d\tilde{\mathbf{u}}}{dt} + L\tilde{\mathbf{u}} = \tilde{\mathbf{f}}_1 + \tilde{\mathbf{f}}_2 \,, \tag{4}$$

where the linearization matrix L and the vectors $\tilde{\mathbf{f}}_1$ and $\tilde{\mathbf{f}}_2$ are given by

$$L = \frac{\partial \mathbf{R}}{\partial \mathbf{U}}, \qquad \tilde{\mathbf{f}}_1 = -\left(\frac{\partial \mathbf{R}}{\partial \mathbf{X}}\tilde{\mathbf{x}} + \frac{\partial \mathbf{R}}{\partial \dot{\mathbf{X}}}\dot{\tilde{\mathbf{x}}}\right), \qquad \tilde{\mathbf{f}}_2 = -\frac{\partial \mathbf{R}}{\partial \mathbf{U_b}}\tilde{\mathbf{u_b}} \,.$$

The unsteady periodic flow could be determined by solving the linear equations (4),
but due to linearity can be decomposed into a sum of complex harmonics of the
form $\tilde{\mathbf{u}}_k(t) = \Re(e^{ik\omega t}\hat{\mathbf{u}}_k)$, each of which can be computed separately. The complex
elements of $\hat{\mathbf{u}}_k$ define the amplitude and phase of the unsteadiness at frequency $k\omega$.
Analogous expansions hold for $\tilde{\mathbf{x}}(t)$, $\dot{\tilde{\mathbf{x}}}(t)$ and $\tilde{\mathbf{u}}_b(t)$. Inserting such expressions in
equation (4) and considering only the mode $k=1$ for simplicity, yields the harmonic
equations

$$(i\omega T + L)\hat{\mathbf{u}} = \hat{\mathbf{f}}_1 + \hat{\mathbf{f}}_2 \,, \tag{5}$$

which can be viewed as the frequency domain counterpart of equations (4). The
linear system (5) is complex and it has size $(N \times N_{eqs})$. The vectors $\hat{\mathbf{f}}_1$ and $\hat{\mathbf{f}}_2$
are its right-hand-side and they give the sensitivity of the residuals to harmonic

deformations of the mesh and to incoming harmonic perturbations respectively. Based on an idea of Ni and Sisto [16], the linear equations are solved with the same pseudo time-marching approach adopted for the solution of the nonlinear steady equations, that is by introducing a fictitious time-derivative $d\hat{\mathbf{u}}/d\tau$ and time-marching the solution of the system of linear ODE's:

$$\frac{d\hat{\mathbf{u}}}{d\tau} = -\left[(i\omega T + L)\hat{\mathbf{u}} - \hat{\mathbf{f}}_1 - \hat{\mathbf{f}}_2\right]$$

until $d\hat{\mathbf{u}}/d\tau$ vanishes. Discretizing this time-derivative leads to the linear fixed-point iteration discussed in greater detail in the following section.

In the flutter case, the object of the analysis is to assess the stability of a particular structural mode. The frequency ω and the blade mode shape are calculated with a finite-element program and used to determine $\hat{\mathbf{f}}_1$, which is non-zero throughout the computational domain since the grid deforms following the harmonic vibration of the blade, whereas $\hat{\mathbf{f}}_2$ is set to zero. The phase between the motion of adjacent blades (Inter-blade Phase-Angle or $IBPA$) is an additional parameter of the analysis. It is given by $\phi_j = 2\pi j/N_{blades}$ and the index j usually called *nodal diameter* can take any integer value between 0 and $(N_{blades} - 1)$, though the critical values are usually the first few ones, as shown in [9]. Equations (5) can then be solved for a single passage, introducing the complex phase shift $e^{i\phi_j}$ between the two periodic boundaries. The output of interest is the net energy flux from the structure to the working fluid over one cycle of vibration, defined by the *worksum* integral

$$W = \int_0^{T_v} \int_S p\mathbf{u}_{blade} \cdot d\mathbf{S}dt \, ,$$

in which T_v is the period of vibration, p and u_{blade} are the time-dependent blade static pressure and velocity respectively, $d\mathbf{S}$ is the elemental blade surface with

9

outward normal and S is the overall blade surface. A positive sign indicates stability as energy is transferred from the structure to the fluid, whereas a negative sign indicates the occurrence of flutter. In the engineering community, the logarithmic decrement δ is a more frequently used stability parameter, which depends on the ratio between the amplitude V of two consecutive cycles of vibration. It is defined as $\delta = V(t + T_v)/V(t)$ and it can be proved that

$$\delta = \frac{W}{\omega^2} \ .$$

In forced response, the object of the analysis is to determine the unsteady forces acting on the blade due to any of the harmonic components, into which the incoming time-periodic gust can be decomposed. The $IBPA$ depends on the geometric properties of the problem. In the case of forcing coming from circumferentially periodic wakes, the blades and the wakes may have different pitches and hence there is a difference in the times at which neighbouring wakes strike neighbouring blades. Therefore the $IBPA$ of the fundamental harmonic is $2\pi N_{wakes}/N_{blades}$. Again the linear harmonic equations (5) can be solved for a single blade passage using complex periodic boundary conditions. The vector $\hat{\mathbf{f}}_1$ is zero throughout the domain because the mesh is stationary and the vector $\hat{\mathbf{f}}_2$ is non-zero only at the inlet or outlet boundaries, where the harmonic perturbation is prescribed. The unsteady aerodynamic force acting on the blade can be calculated in a post-processing step for each structural mode using the unsteady pressure field determined with the harmonic analysis.

The linear unsteady analysis is completed by enforcing suitable linearized boundary conditions. The inflow, outflow and (complex) periodic boundary conditions can all be symbolically included into equations (5). Taking into account

10

the linearized strong wall boundary condition, however, the system to be solved becomes:

$$
\begin{aligned}
(I-B)\left[(i\omega T + L)\hat{\mathbf{u}} - \hat{\mathbf{f}}_1 - \hat{\mathbf{f}}_2\right] &= 0 \\
B\,\hat{\mathbf{u}} &= \hat{\mathbf{u}}_{wall}\,.
\end{aligned}
\tag{6}
$$

The component $\hat{\mathbf{u}}_{wall}$ of the linear flow velocity at the wall is zero for both inviscid and viscous walls in the forced response problem as the grid does not deform, while it is non-zero for both wall types in the flutter problem, due to the surface displacements and in the inviscid case also to the rotation of the wall normals [15]. The implementation of the inflow and outflow boundary conditions is based on one-dimensional nonreflecting boundary conditions [17]. Equations (6) are then solved using the same preconditioned pseudo time-marching method as for the nonlinear equations.

4   GMRES stabilization

The linearized harmonic NS equations (6) can be viewed as a simple linear system of the form

$$
A\mathbf{x} = \mathbf{b}\,.
\tag{7}
$$

Though equations (6) are complex, *hydlin* has been written using real arithmetic, that is considering real vectors of size $(2 \times N_{eqs} \times N)$ with the factor 2 accounting for real and imaginary part, rather than complex vectors of size $(N_{eqs} \times N)$. This choice has been made because of errors often introduced by highly optimized FORTRAN compilers when dealing with complex arithmetic. Therefore the system (7) also has dimension $(2 \times N_{eqs} \times N)$ and the code for its solution can be regarded as the

11

fixed-point iteration:

$$\mathbf{x}_{n+1} = (I - M^{-1}A)\mathbf{x}_n + M^{-1}\mathbf{b} \,, \tag{8}$$

in which M^{-1} is a preconditioning matrix resulting from the Runge-Kutta time-marching algorithm, the Jacobi preconditioner and one multigrid cycle. Linear stability analysis of (8) shows that necessary condition for its convergence is that all the eigenvalues of $(I - M^{-1}A)$ lie within the unit circle centred at the origin in the complex plane or equivalently that all the eigenvalues of $M^{-1}A$ lie in the unit disc centred at $(1, 0)$. For most aeroelastic problems of practical interest, this condition is fulfilled and the linear code converges without difficulty. However an exponential growth of the residual has been encountered in situations in which the steady flow calculation itself failed to converge to a steady-state but instead finished in a small-amplitude limit cycle, related to some physical phenomenon such as separation bubbles, corner stalls and vortex shedding at a blunt trailing edge. The solution procedure of the nonlinear steady equations (3) is not time-accurate because of the local time-stepping technique and the Jacobi preconditioner used for the integration, but it nevertheless reflects some physical properties of the flow field due to the pseudo time-marching strategy associated with the Runge-Kutta algorithm. Physical small-amplitude limit cycles do not prevent the steady solver from converging to an acceptable level, although their effect is sometimes visible in small oscillations of the residual. However they result in a small number of complex conjugate pairs of eigenvalues of the linearization matrix $(I - M^{-1}A)$ lying outside the unit circle (*outliers*) and thus causing the exponential growth of the residual of the linear equations. This problem has been overcome by implementing a preconditioned GMRES algorithm in *hydlin*. GMRES is an iterative method for

12

the solution of linear systems, belongs to the family of Krylov subspace methods [13] and is guaranteed to converge even in the presence of outliers. The Krylov subspace of dimension m generated by the preconditioned operator $M^{-1}A$ and the vector $M^{-1}\mathbf{b}$ is the vectorial space spanned by the vectors $((M^{-1}A)^j M^{-1}\mathbf{b}, \ j = 0, \ldots m-1)$, that is

$$K_m = < M^{-1}\mathbf{b}, \ (M^{-1}A)M^{-1}\mathbf{b}, \ \ldots, \ (M^{-1}A)^{m-1}M^{-1}\mathbf{b} > .$$

The GMRES algorithm is based on the progressive reduced Arnoldi factorization [13] of $M^{-1}A$:

$$M^{-1}AQ_m = Q_{m+1}\tilde{H}_m , \qquad (9)$$

where m is the current iteration, $\tilde{H}_m$ is a Hessemberg matrix of size $((m+1) \times m)$, Q_m is a matrix of size $((2 \times N_{eqs} \times N) \times m)$ whose m columns $\mathbf{q}_j$ $(j = 1, \ldots, m)$ form an orthonormal basis for the Krylov subspace K_m and Q_{m+1} is Q_m augmented with a new Krylov vector $\mathbf{q}_{m+1}$. Denoting by $h_{j,m}$ $(j = 1, \ldots, m)$ the elements of the mth column of $\tilde{H}_m$, the mth column of equation (9) can be written as:

$$M^{-1}A\mathbf{q}_m = h_{1,m}\mathbf{q}_1 + \ldots + h_{m+1,m}\mathbf{q}_{m+1} , \qquad (10)$$

which shows that $\mathbf{q_{m+1}}$ satisfies an $(m+1)-$term recursive relation involving itself and the previous m Krylov vectors. It should be noted that the size of each $\mathbf{q_j}$ is equal to that of the complex linear flow field. At the mth GMRES iteration the solution of (7) is approximated by the linear combination of the m $\mathbf{q_j}$'s which minimizes the 2-norm of the residual $\mathbf{r}_m = M^{-1}(\mathbf{b} - \mathbf{Ax_m})$ and is thus given by $\mathbf{x}_m = \mathbf{x}_{start} + Q_m\mathbf{t}_m$, in which $\mathbf{x}_{start}$ is the initial solution and $\mathbf{t}_m$ is the column vector containing the m coefficients of the linear combination. For this reason the algorithm can be viewed as an optimization process.

13

The implementation of the preconditioned GMRES solver in *hydlin* has been carried out at the top routine level. At this level, the pseudo-code of the preconditioned multigrid iteration without GMRES looks like:

$$\mathbf{x} = \mathbf{x}_{start}$$

$$\mathbf{x} = \mathrm{mg}(A, \mathbf{x}, \mathbf{b}, n_{cl})$$

$$\mathbf{x}_{finish} = \mathbf{x}$$

where 'mg' is the core routine which performs the preconditioned fixed-point iteration (8) and $\mathbf{x}_{finish}$ is the solution after n_{cl} multigrid cycles. The GMRES solver does not require any change to 'mg' and uses it as a black-box to determine the preconditioned Krylov vectors $M^{-1}A\mathbf{q}_j$. The computationally cheap minimization is also carried out at the top routine level and the pseudo-code of the main *hydlin* using GMRES is:

$$\mathbf{q}_1 = \mathrm{mg}(A, \mathbf{x}_{start}, \mathbf{b}, n_{cl}) - \mathbf{x}_{start}; \qquad \mathbf{q}_1 = \mathbf{q}_1/|\mathbf{q}_1|$$

for $m = 1 : n_{Kr}$

$\quad M^{-1}A\mathbf{q}_m = -\mathrm{mg}(A, \mathbf{q}_m, \mathbf{0}, n_{cl}) + \mathbf{q}_m$

$\quad \mathbf{q}_{m+1}$ from equation (10); $\qquad \mathbf{q}_{m+1} = \mathbf{q}_{m+1}/|\mathbf{q}_{m+1}|$

$\quad$ determine $\mathbf{t}_m$ which minimizes $\mathbf{r}_m$

end

$$\mathbf{x}_{finish} = \mathbf{x}_{start} + Q_{n_{Kr}}\mathbf{t}_{n_{Kr}}$$

The first Krylov vector $\mathbf{q}_1$ is the normalized residual of the preconditioned system, n_{Kr} is the overall number of GMRES iterations and n_{cl} is the number of multigrid cycles per GMRES iteration. Note that the right-hand-side of (7) is set to zero before using 'mg' to determine $M^{-1}A\mathbf{q}_m$. The numerical solution of the optimization

14

problem of dimension m which leads to $\mathbf{t_m}$ is described in [13]. The value of n_{Kr} required for full convergence is much smaller than the size of A, but nevertheless very big with respect to the computing resources usually available. This is due to the fact that at the mth iteration all m $\mathbf{q_j}$'s are needed to compute the new orthogonal vector of the basis. This problem is overcome using the *restart* option, that is performing n_{Kr} iterations and re-starting GMRES from the updated solution re-computing from there a new set of n_{Kr} Krylov vectors. This is achieved by wrapping the inner loop described above with an outer one which restarts GMRES each time. Values of n_{Kr} between 10 and 30 make the computation affordable even for large problems and a good convergence level is usually achieved within 20 restarted cycles. Unfortunately the restarted solver may lead to numerical stagnation of the residual [13]. Extensive numerical validation on a variety of turbomachinery test cases, however, has highlighted that this can be avoided provided that both n_{Kr} and n_{cl} are chosen above certain case dependent threshold values. Including the extra CPU-time required for the matrix-vector products and the minimization process of GMRES in the cost of one multigrid cycle, the CPU-time for executing a given number of multigrid cycles using GMRES is only from 1 to 3 % higher than using the standard iteration. The additional burden associated with GMRES is the extra memory allocation for the n_{Kr} Krylov vectors. It should also be noted that different choices of n_{cl}, as well as other multigrid parameters such as the number of iterations on the different grids, lead to a different preconditioner M^{-1} and therefore they play a crucial role in determining the overall number of multigrid cycles to achieve the desired convergence level. The experience gained so far has shown that a) the convergence rate (slope of the curve residual vs. number of multigrid

15

cycles) always increases with n_{Kr} and b) there exist values of n_{cl} which maximize it. The upper threshold of n_{Kr} is usually fixed by the available computing resources.

Another advantage of GMRES is that it allows the straightforward determination of the unstable eigenmodes, as the algorithm has the property of solving the least stable modes first, namely those whose eigenvalues are farthest from the centre of the unit circle in the complex plane. As shown in the next section, this enables one to relate the source of numerical instability to the physical unsteadiness which causes it. In order to establish the relationship between the least stable modes and the set of Krylov vectors, let us start by considering the partial reduction of $M^{-1}A$ based on the mth Krylov subspace:

$$Q_m^H M^{-1} A Q_m = H_m \, , \tag{11}$$

where H_m denotes the upper $(m \times m)$ portion of $\tilde{H}_m$ and the superscript ^{H} the Hermitian conjugate operator. The eigenvalues θ_j of H_m are called Ritz values and they are defined by

$$H_m \mathbf{y}_j = \theta_j \mathbf{y}_j, \qquad j = 1, 2, \ldots, m \tag{12}$$

where $\mathbf{y_j}$ is the right eigenvector of H_m associated with θ_j. Combining equations (11) and (12) yields

$$Q_m^H M^{-1} A Q_m \mathbf{y}_j = (Q_m^H Q)\theta_j \mathbf{y}_j \, , \tag{13}$$

and consequently

$$Q_m^H (M^{-1}A - \theta_j I) Q_m \mathbf{y}_j = 0 \, . \tag{14}$$

The m vectors

$$Q_m \mathbf{y}_j = \sum_{l=1}^{m} (y_j)_l \mathbf{q}_l \qquad j = 1, 2, \ldots, m \tag{15}$$

16

are the Ritz vectors of A based on the mth Krylov subspace, which provide an approximate estimate of the sought dominant or least stable eigenmodes. In fact, equation (14) states only that the residual of each eigenvector $\mathbf{res}_{eig} = (M^{-1}A - \theta_j I)Q_m\mathbf{y_j}$ is orthogonal to the subspace K_m, but the expression (15) would provide the exact eigenmodes only if $\mathbf{res}_{eig} = 0$. It can be proved, however, that the 2-norm of $\mathbf{res}_{eig}$ depends linearly on the residual of the linear equations. For all the test cases considered, 150 GMRES iterations without restart have been sufficient to achieve a good convergence level of the linear equations and therefore to obtain an accurate estimate of the dominant modes.

Finally, it should be noted that the most appropriate definition of the flow field determined by solving the nonlinear equations in the presence of small limit cycles which then generate the linear instabilities would be 'base' or 'background' flow. Nevertheless the adjectives 'mean' and 'steady' are sometimes used as synonyms in this paper, underlining the fact that such flow field has been computed with a numerical approach suitable for the solution of the steady flow equations.

5 Results

5.1 Two-dimensional turbine section

One of the test cases that has been used for both assessing the predictive capabilities of *hydlin* and testing the implemented GMRES solver is the 2D turbine section of the 11th Standard Configuration, which is the mid-span blade-to-blade section of an annular turbine cascade with 20 blades. The annular test-rig and cascade geometry are briefly described in reference [18], which also provides experimental

17

measurements and various computed results of the steady and unsteady flow field due to blade-plunging with prescribed $IBPA$. Two steady working conditions are considered: a subsonic one with exit Mach number of 0.68 and a transonic one with exit Mach number of 0.96. The computational grid that we have used for the investigation is a quasi-orthogonal H-type mesh with medium refinement: it has 273 nodes in the streamwise and 65 nodes in the pitchwise direction, for a total of 17745 grid nodes. A preliminary mesh-refinement analysis carried out using a coarser 7869-node (183×43) and finer 39673-node (409×97) mesh has shown no difference of practical interest between the results obtained with the medium and finer grids. The coarser mesh is shown in figure 1 while figure 2 provides measured and computed steady isentropic Mach number M_{is} on the blade surface for the two working conditions. The variable on the x-axis is the nondimensional position along the true blade chord c. The high pressure patch at about 20 % chord and the rapid pressure rise at about 80 % chord on the suction surface in the transonic case (figure 2-b) are due to a separation bubble and an impinging shock respectively. This is clearly visible in the Mach number contours of figure 3, which also show how both the blade boundary layers and wakes thicken after passing through the shock. Figure 4 provides measured and computed amplitude and phase of the first harmonic of the unsteady pressure coefficient c_p. Its definition is:

$$c_p = \frac{\hat{p}}{(p_{01} - p_1)} \frac{c}{h} \, ,$$

where $\hat{p}$ is the complex amplitude of the linear unsteady pressure on the blade surface, p_{01} and p_1 are the mass-averaged inlet total and static pressure respectively and h is the bending amplitude. For both working conditions, large differences between measured and computed results are visible on the suction surface where most

of the unsteady phenomena take place. However the numerical results presented in this paper are in very good agreement with those in the literature [18, 8].

The stability curves (δ *vs.* $IBPA$) for both flow regimes are provided in figure 5-a, which shows that the system never becomes aeroelastically unstable. The nonlinear calculations of both the subsonic and transonic base flow converge without difficulties to machine epsilon (10^{-18}). However all the linear calculations based on the transonic base flow diverge using the standard code and convergence can be retrieved only using GMRES, as shown in the convergence histories of *hydlin* in figures 5-b and 5-c, which refer to $IBPA = 180^o$. In both figures the variable on the x-axis is the number of multigrid cycles and that on the y-axis is the logarithm in base 10 of the root-mean-square of all nodal residuals (rms). The number at the right of the label 'GMRES' in the legend is n_{Kr}. Figure 5-b illustrates the effect of n_{cl} on the convergence histories of GMRES 20: among the 4 values tried for this test case the minimum overall number of multigrid cycles or equivalently of CPU-time required for dropping the residual below -8 is obtained for $n_{cl} = 3$ and $n_{cl} = 10$. All the GMRES convergence histories in figure 5-c refer to $n_{cl} = 3$ and they highlight that the convergence rate increases monotonically with n_{Kr} in the range of practical interest. All linear calculations based on the subsonic flow regime converge also without GMRES and the convergence histories of the linear code ($IBPA = 180^o$) using the standard iteration and GMRES 20 are provided in figure 5-d. The memory requirements with 3 grid levels for the multigrid scheme are 52 and 86 Mbytes respectively. Both calculations have been started from the same initial solution and run on 8 processors of a computer cluster consisting of 24 four-processor Sun Ultra-80 nodes, with a Sun Blade-1000 front-end. The 700

19

iterations for achieving a residual level of -17.5 with GMRES have been carried out in about 27 minutes of CPU-time, whereas the 1800 needed to obtain the same level with the standard iteration have required 69 minutes.

In order to investigate the origin of the numerical instability of the standard code for transonic flow conditions, the first 150 dominant eigenmodes of the pre-conditioned linearization matrix $M^{-1}A$ for $n_{cl} = 1$ have been determined using the procedure described in the previous section and they are plotted in the complex plane of figure 6. The two complex conjugate pairs of outliers labelled with 1 and 2 are responsible for the exponential growth of the residual associated with the fixed-point iteration (8). In fact, its asymptotic convergence rate is determined by the spectral radius ρ of the linear operator $M^{-1}A$ and it can be proved that the relationship between the asymptotic slope of the residual curve and ρ is:

$$\frac{\Delta\left(\log(rms)\right)}{N_{mg}} \approx \log\rho \, , \tag{16}$$

where N_{mg} is the number of multigrid cycles across which the variation of rms is considered. This equation provides the theoretical relationship between the slope of the exponentially growing residual curve of the standard iteration (figures 5-b and 5-c) and the spectral radius of the linear operator (radius of the outlier 1). Inserting the computed values in it yields $46.90e{-}3 \approx 47.53e{-}3$, which demonstrates the correctness of the mathematical analysis. Figure 7-a shows that the maximum pressure amplitude of the eigenvector associated with the complex conjugate pair of outliers 1 occurs at the edge of the separation bubble on the suction surface and this proves that the origin of the numerical instability is the small limit cycle associated with this unstable separation. The eigenmode associated with the outlier 2 also corresponds to the separation on the suction surface and therefore is not

20

reported here. The pressure amplitude of the eigenvector associated with the complex conjugate pair of eigenvalues 3 is provided in figure 7-b. Nonzero amplitudes occur both in the shock and the separation bubble. The eigenvalues of this mode lie in the unit disk, but they would be responsible for a very low convergence rate of the standard code in the absence of any outlier because of their proximity to the unit circle. It has also been found that the two dominant eigenmodes described above are independent of the $IBPA$, despite the fact that $M^{-1}A$ depends on it. This phenomenon is probably due to the high spatial localization of the unstable modes and is highlighted in table 1, which reports the real and imaginary parts of the first 3 least stable modes for 3 different $IBPA$'s. This feature can be exploited by 'hybrid' solvers such as the *Recursive Projection Method* [19]. This algorithm uses Newton's method for determining the projection of the solution on the small unstable eigenspace associated with the few outliers and the standard fixed-point iteration for calculating the projection of the solution on the bigger space associated with the remaining modes. In this way, the unstable eigenspace does not need to be recomputed for each $IBPA$. The independence of the unstable eigenspace on the $IBPA$, however, cannot be exploited by GMRES.

5.2 Three-dimensional fan

The second test case considered is a three-dimensional fan rotor whose geometry and surface grid are shown in figure 8. This grid has only 157441 nodes and is quite coarse, but all the phenomena discussed in this section have been also observed with finer computational meshes and for other test cases. The linear flutter analysis has been carried out for 4 points of a constant-speed working line using *hyd* and

IBPA (^{o})	mode	$\Re(\lambda)$	$\Im(\lambda)$
36	1	0.640143	0.984962
	2	0.665552	0.992178
	3	0.004075	0.004150
180	1	0.640016	0.984956
	2	0.665476	0.992322
	3	0.004076	0.004150
270	1	0.639930	0.984763
	2	0.665644	0.992444
	3	0.004075	0.004150

Table 1: First 3 dominant eigenvalues for 3 different $IBPA$'s.

hydlin. The computed pressure ratio β is plotted versus the computed mass flow $\dot{m}$ in figure 9-a. Their definition is:

$$\beta = \frac{p_{02}}{p_{01}}, \qquad \dot{m} = \int_{S_2} \rho_2 \, \mathbf{u}_2 \cdot d\mathbf{S}_2 \ .$$

All variables in the two expressions above refer to the base flow: p_{01} and p_{02} are respectively the inlet and outlet mass-averaged total pressure, S_2 is the area of the outlet boundary, ρ_2 is the outlet density and $\mathbf{u}_2$ is the outlet velocity vector. Note that the values of both β and $\dot{m}$ in figure 9-a are given as percentage deviations from their design values. For all 4 working conditions the residual of the nonlinear steady equations drops by four orders of magnitude (figure 9-b), ending in a low-amplitude limit cycle.

22

The analysis of the flutter stability of the first flap mode has been carried out for all 4 working conditions and the computed logarithmic decrement is plotted in figure 10. As expected, the least stable aeroelastic modes are those associated with the first few $IBPA$'s and the blades undergo flutter in the 2 nodal diameter mode at the base flow conditions D, which are the closest to stall. All linear calculations have been performed using GMRES, as they were otherwise unstable. This is visible in the convergence plots of $hydlin$ reported in figure 11, which refer to the base flow conditions D and to $IBPA = 180^o$. Figure 11-a shows that the GMRES solver stagnates if $n_{cl} = 1$ and an acceptable convergence rate can be achieved only using $n_{cl} = 3$ and $n_{Kr} \geq 30$. The GMRES solver does not stagnate using $n_{Kr} = 100$ with either values of n_{cl}, but a better convergence rate is obtained with $n_{cl} = 3$ (figure 11-b). It should be noted that solving the linear equations about a 'pseudo time-averaged' base flow, obtained by averaging the nonlinear solution over one numerical limit cycle of hyd, has not removed the instability of the linear calculations using the standard iteration. It might be more appropriate to linearize the flow unsteadiness either about the 'stabilized' solution of the nonlinear equations, determined by using GMRES [20] or about the true time-averaged flow. This can be obtained either by introducing unsteady stress terms in the nonlinear equations [21] or solving the time-dependent nonlinear equations and then time-averaging the flow solution. It is the authors' view, however, that these approaches would also not remove the linear instabilities of the standard linear solver. In fact, the limit cycles under discussion are stable and the theory of dynamical systems foresees that the underlying steady solutions are unstable [22] leading to the exponential growth of their linear perturbations. Figure 11-b also highlights that starting GMRES from

the last solution of the standard *hydlin* after the calculation has diverged, results in an initially sharp reduction of the residual and then in a convergence rate similar to that of the descending branch of the standard code. This behaviour can be explained by the presence of a few outliers: after a few hundred multigrid cycles needed to resolve the stable modes, the unstable modes associated with the outliers become dominant and determine the exponential growth of the residual of the standard iteration. They are instead solved very rapidly restarting the calculation with GMRES. In fact, the subset of the spectrum of $M^{-1}A$ with the first 150 dominant eigenvalues has 4 complex conjugate pairs of outliers, labelled from 1 to 4 in order of decreasing distance from the centre of the unit disc in figure 12, which refers to $n_{cl} = 1$. Inserting in equation (16) the computed data relative to the slope of the ascending branch of the residual curve of the standard iteration (figure 11) and the spectral radius of $M^{-1}A$ (radius of the outlier 1) yields $38.82e{-3} \approx 40.17e{-3}$, which confirms once more the correctness of the mathematical analysis.

The eigenmode associated with the pair of outliers 1 is due to the hub corner stall, since its maximum pressure amplitude occurs in a small region between the suction side and the hub close to the Trailing Edge (TE) as shown in figure 13-a. Contours of the same variable in a blade-to-blade section close to the hub are presented in figure 13-b, while a two-dimensional view of the flow separation caused by the corner stall is given in figure 13-c, which shows the velocity vectors in the same blade-to-blade section. The eigenmode associated with the pair of outliers 3 corresponds to a separation bubble on the suction side close to the Leading Edge (LE) in the hub region. The eigenmodes 2 and 4 correspond to the same flow phenomena as 1 and 3 respectively. The numerical instabilities of the standard code

24

are therefore due to the linearization of the small-amplitude limit cycles associated with the hub corner stall and the LE separation.

The eigenmode corresponding to the complex conjugate pair 5 does not cause the exponential growth of the residual as it lies in the unit disc, but it would be responsible for a very low convergence rate of the standard code in the absence of any outlier because of its proximity to the unit circle, as discussed in [19]. This eigenmode contains traces of the previous 4 and corresponds also to a shock on the suction side close to the tip. Similarly to the turbine test case, the dominant eigenmodes described above have been found to be independent of the $IBPA$ and this might be due again to their high spatial localization.

All calculations have been run with 4 grid levels for the multigrid scheme on the SUN cluster described in the previous section. The CPU-time of one multigrid cycle depends on the number of iterations performed on each grid level. The values chosen for this test case have led to a CPU-time of about 56 seconds for one multigrid cycle of $hydlin$ using 8 processors, and the 800 cycles needed for a good convergence of each linear calculation have thus required an overall time of about 12 hours. By comparison, the CPU-time for one multigrid cycle of hyd is about half of that needed by $hydlin$.

6 Conclusions

This paper has presented the linear analysis of turbomachinery aeroelasticity from a simple algebraic viewpoint, which allows one a relatively straightforward understanding of the relationship between the numerical instabilities of the linearized

solver of the Navier-Stokes equations and the small unsteady phenomena of the base flow field. The implementation of the GMRES algorithm in the existing linear NS solver based on a preconditioned fixed-point iteration has stabilized the code, allowing the aeroelastic analysis to be carried out even in presence of small unsteady phenomena in the base flow, which are believed not to have any significant effect on the aeroelastic behaviour of the component under investigation. The CPU-time required for one multigrid cycle in the GMRES solver is only from 1 to 3 % higher than using the standard iteration. The overall number of multigrid cycles needed to achieve a given level of convergence with the restarted GMRES algorithm depends on both the number of GMRES iterations per restarted cycle and the number of multigrid cycles per GMRES iterations. Increasing the former parameter always improves the convergence rate, whereas optimal case dependent values seem to exist for the latter one. The convergence rate of the GMRES iteration also depends on other multigrid parameters, such as the number of iteration on the different grid levels. For test cases without unstable modes the same convergence level can be obtained in considerably fewer iterations by using the GMRES rather than the standard solver. The extra memory allocation associated with GMRES 10 and GMRES 30 are about 35 and 100 % of that used by the standard fixed-point iteration respectively. Both the correctness of the analysis and the relationship between numerical instabilities of the linear solver and unsteady phenomena of the base flow have been demonstrated through the linear flutter analysis of two realistic turbomachinery test cases.

Acknowledgements

References

[1] Verdon, J.M., "Review of unsteady aerodynamic methods for turbomachinery aeroelastic and aeroacoustic applications," *AIAA Journal*, Vol. 31, No. 2, 1993, pp. 235–250.

[2] Verdon, J.M. and Caspar, J.R., "A linearized unsteady aerodynamic analysis for transonic cascades," *Journal of Fluid Mechanics*, Vol. 149, Dec. 1984, pp. 403–429.

[3] Hall, K.C., "Deforming grid variational principle for unsteady small disturbance flows in cascades," *AIAA Journal*, Vol. 31, No. 5, 1993, pp. 891–900.

[4] Marshall, J.G. and Imregun, M., "A review of aeroelasticity methods with emphasis on turbomachinery applications," *Journal of Fluid and Structures*, Vol. 10, 1996, pp. 237–267.

[5] Hoyniak, D. and Clark, W.S., "Aerodynamic damping predictions using a linearized Navier-Stokes analysis", ASME Paper 99-GT-207, June 1999.

[6] Clark, W.S. and Hall, K.C., "A time-linearized Navier-Stokes analysis of stall flutter," *Journal of Turbomachinery*, Vol. 122, No. 3, July 2000, pp. 467–476.

[7] Hall, K.C., Clark, W.S. and Lorence, C.B., "A linearized Euler analysis of unsteady transonic flows in turbomachinery," *Journal of Turbomachinery*, Vol. 116, No. 3, July 1994, pp. 477–488.

[8] Sbardella, L. and Imregun, M., "Linearized unsteady viscous turbomachinery flows using hybrid grids," *Journal of Turbomachinery*, Vol. 123, No. 3, July 2001, pp. 568–582.

[9] Campobasso, M.S. and Giles, M.B., "Analysis of the effect of mistuning on turbomachinery aeroelasticity," *Proceedings of the IX International Symposium on Unsteady Aerodynamics, Aeroacoustics and Aeroelasticity in Turbomachines*, Presses Universitaires de Grenoble, Grenoble, France, December 2001, pp. 885–896.

[10] Moinier, P., Müller, J.D. and Giles, M.B., "Edge-based multigrid and preconditioning for hybrid grids," *AIAA Journal*, Vol. 40, No. 10, 2002, pp. 1954–1960.

[11] Duta, M.C., Giles, M.B. and Campobasso, M.S., "The harmonic adjoint approach to unsteady turbomachinery design," *International Journal for numerical methods in fluids*, Vol. 40, October 2002, pp. 323–332.

[12] Giles, M.B., Duta, M.C., Müller, J.D. and Pierce, N.A., "Algorithm developments for discrete adjoint methods," *AIAA Journal*, Vol. 41, No. 2, 2003, pp. 198–205.

[13] Saad, Y., "GMRES: a generalized minimal residual algorithm for solving nonsymmetric linear systems," *SIAM Journal on Scientific and Statistical Computing*, Vol. 7, No. 3, 1986, pp. 856–869.

[14] Moinier, P., "Algorithm developments for an unstructured viscous flow solver," Ph.D. Dissertation, Oxford University Computing Laboratory, Oxford University, Oxford, England, UK, December 1999.

[15] Duta, M.C., "The use of the adjoint method for the minimization of forced response," Ph.D. Dissertation, Oxford University Computing Laboratory, Oxford University, Oxford, England, UK, March 2001.

[16] Ni, R.H. and Sisto, F., "Numerical computation of nonstationary aerodynamics of flat plate cascades in compressible flow," *ASME Journal of Engineering for Power*, Vol. 98, No. 2, 1976, pp. 165–170.

[17] Giles, M.B., "Nonreflecting boundary conditions for Euler equation calculations," *AIAA Journal*, Vol. 28, No. 12, 1990, pp. 2050–2058.

[18] Fransson, T.H., Joeker, M., Boelcs, A. and Ott, P, "Viscous and inviscid linear/nonlinear calculations versus quasi three-dimensional experimental cascade data for a new aeroelastic turbine standard configuration," *Journal of Turbomachinery*, Vol. 121, No. 4, October 1999, pp. 717–725.

[19] Campobasso, M.S. and Giles, M.B., "Stabilization of a linearized Navier-Stokes solver for turbomachinery aeroelasticity," *Proceedings of the II International Conference on Computational Fluid Dynamics*, Springer–Verlag, Heidelberg, Germany, 2003,

[20] Pueyo, A. and Zingg, D.W., "Efficient Newton-Krylov Solver for Aerodynamic Computations ," *AIAA Journal*, Vol. 36, No. 11, 1998, pp. 1991–1997.

[21] Ning, W. and He, L., "Some Modelling Issues on Trailing-Edge Vortex Shedding," *AIAA Journal*, Vol. 39, No. 5, 2001, pp. 787–793.

[22] Glendinning, P., "Stability, Instability and Chaos," *Bifurcation theory: stationary points*, Cambridge University Press, Cambridge, 1994, pp. 224–246.
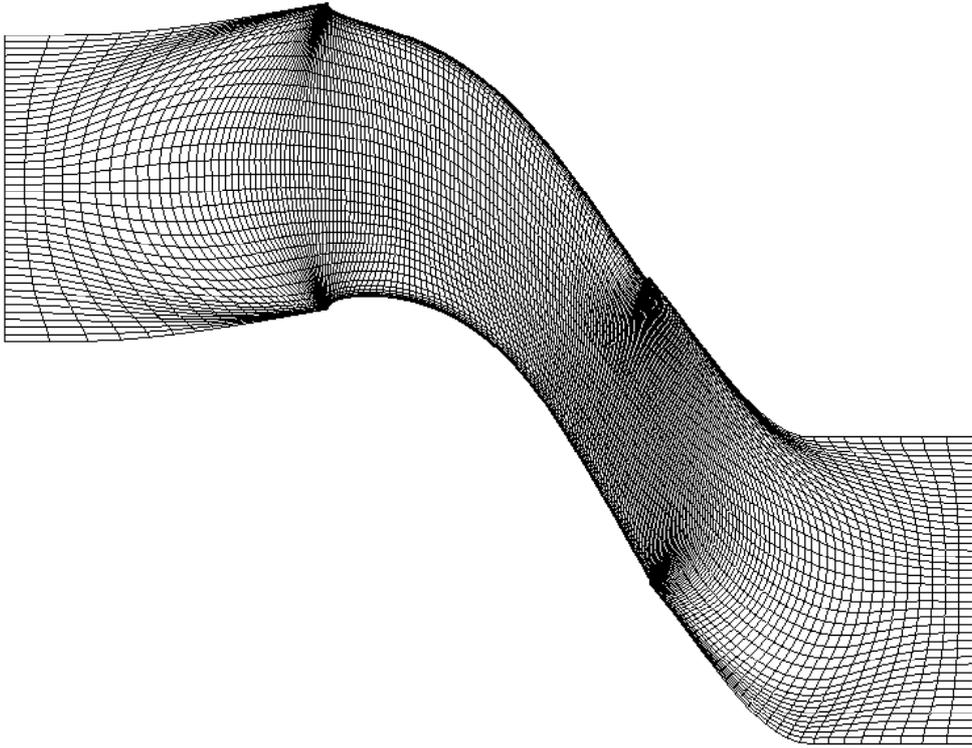
Figure 1: Mesh for the 2D turbine section.

a)

b)
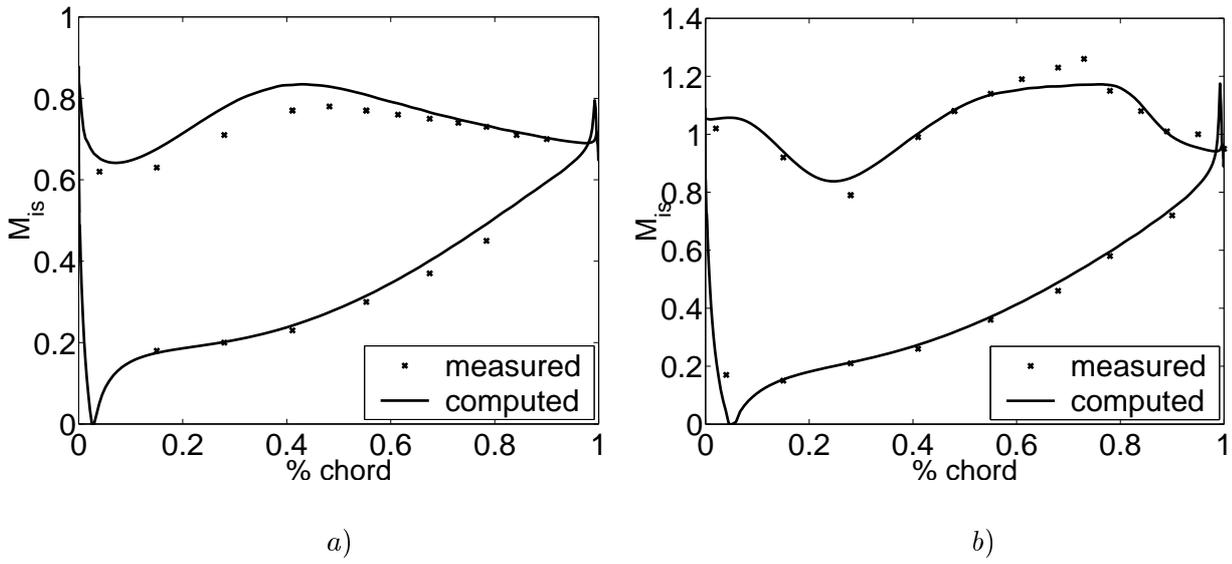
Figure 2: Isentropic Mach number on the blade surface of the 2D turbine: a) subsonic conditions and b) transonic conditions.
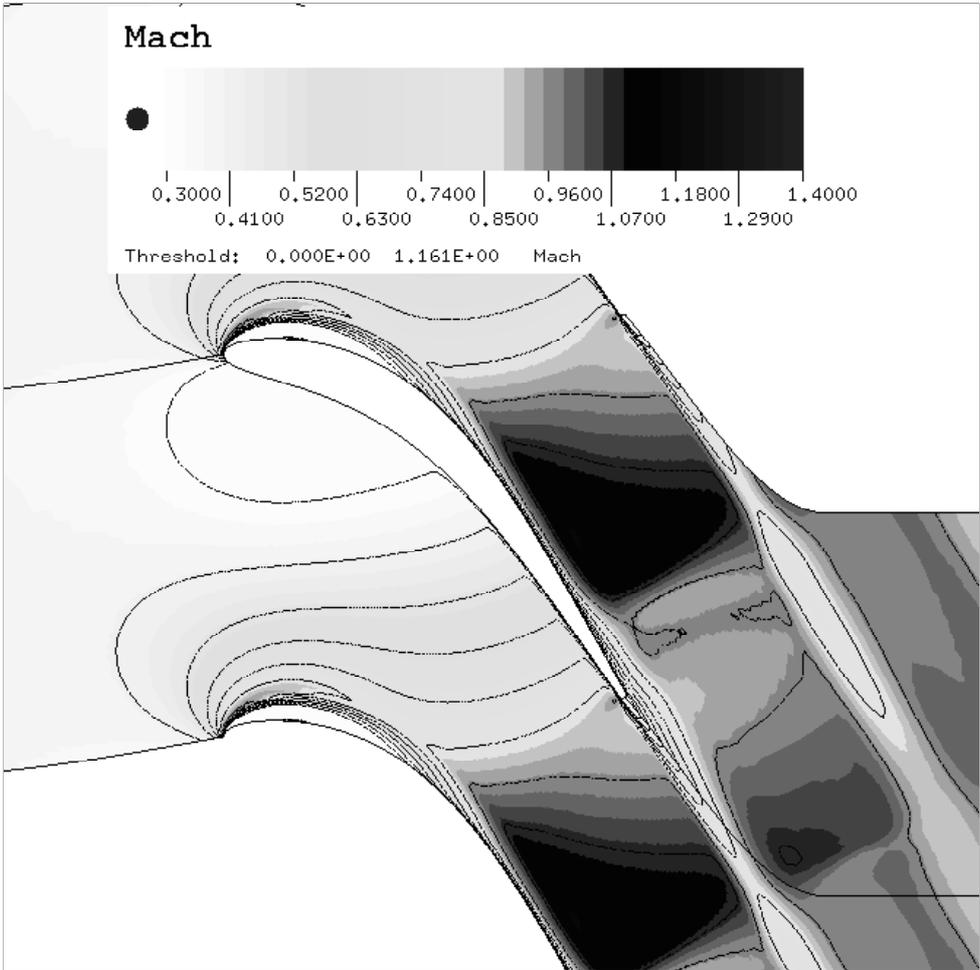
Figure 3: Mach contours for transonic conditions of the 2D turbine.
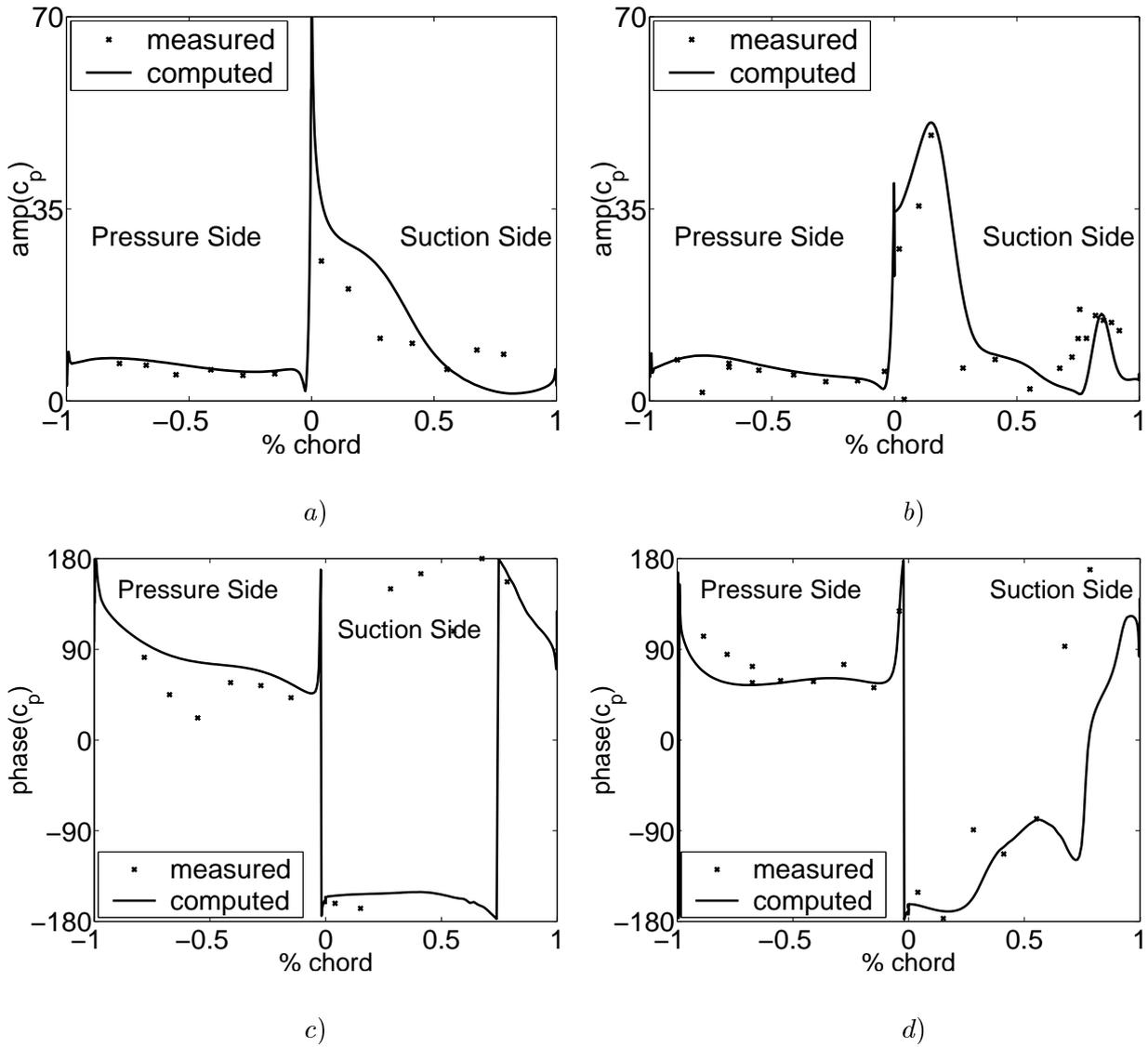
Figure 4: Unsteady pressure coefficient c_p on the blade surface of the 2D turbine: a) amplitude of c_p for subsonic conditions, b) amplitude of c_p for transonic conditions, c) phase of c_p for subsonic conditions and d) phase of c_p for transonic conditions. All results refer to $IBPA = 180^o$.
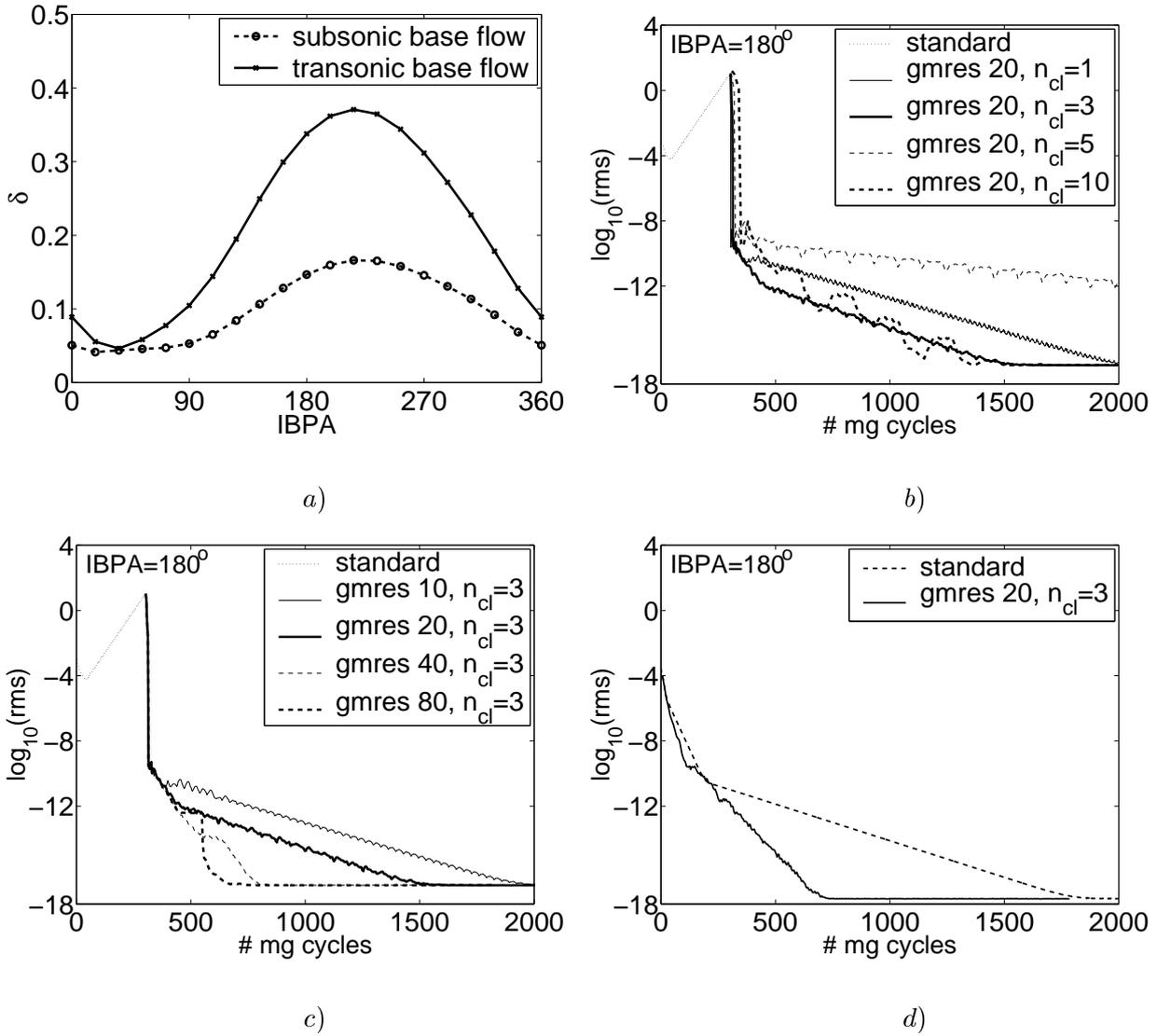
Figure 5: Flutter analysis of the 2D turbine: a) logarithmic decrement versus $IBPA$, b) effect of n_{cl} on GMRES convergence rate (transonic base flow), b) effect of n_{Kr} on GMRES convergence rate (transonic base flow) and d) convergence histories with standard and GMRES iteration (subsonic base flow).
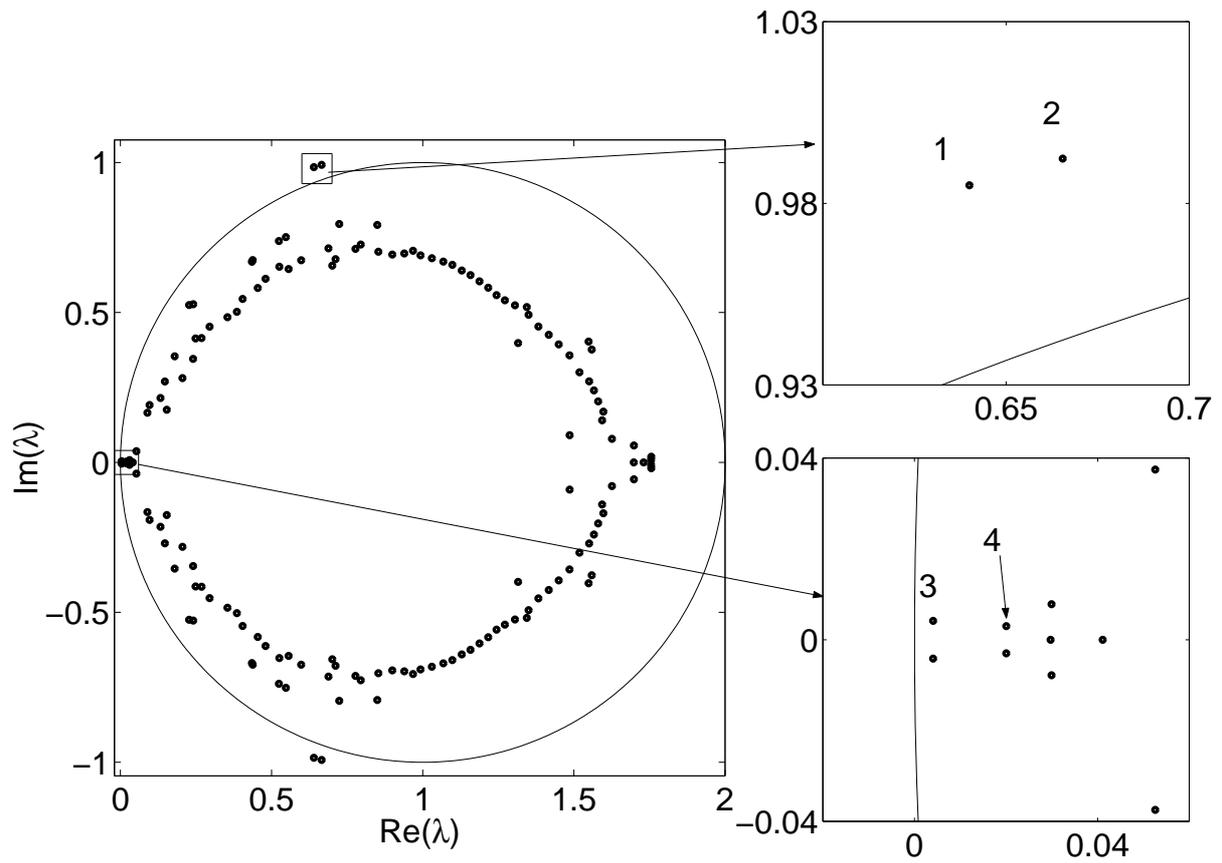
Figure 6: Flutter analysis of the 2D turbine: first 150 dominant eigenvalues of $M^{-1}A$ $(n_{cl}\!=\!1)$ for transonic mean flow and $IBPA\!=\!180^o$.

a)   b)
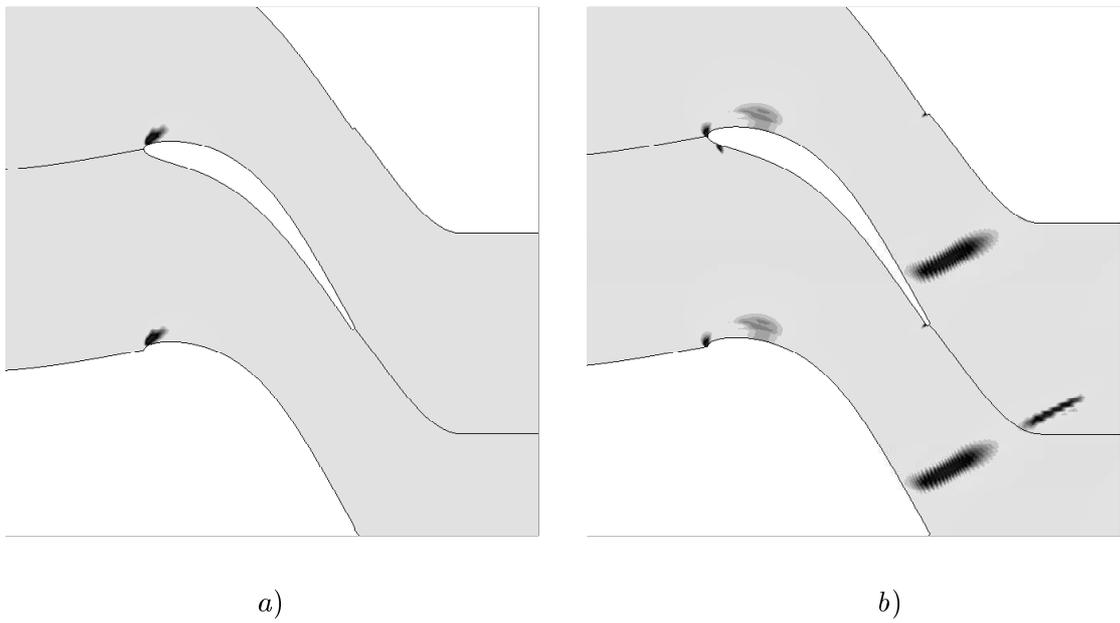
Figure 7: Pressure amplitude of dominant eigenmodes: a) eigenvector associated with the outlier 1 and b) eigenvector associated with the eigenvalue 3.

Figure 8: Blade geometry and surface mesh of the 3D fan.

a)   *b)*
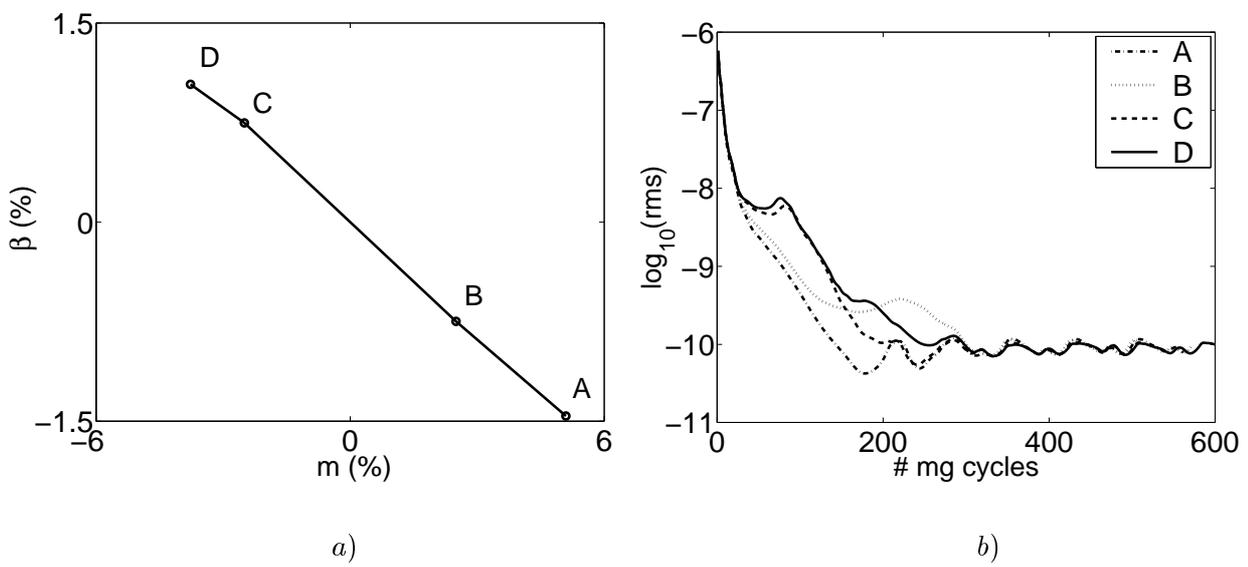
Figure 9: *a)* Constant speed working-line of the 3D fan and *b)* convergence histories of *hyd* for 4 working-points.
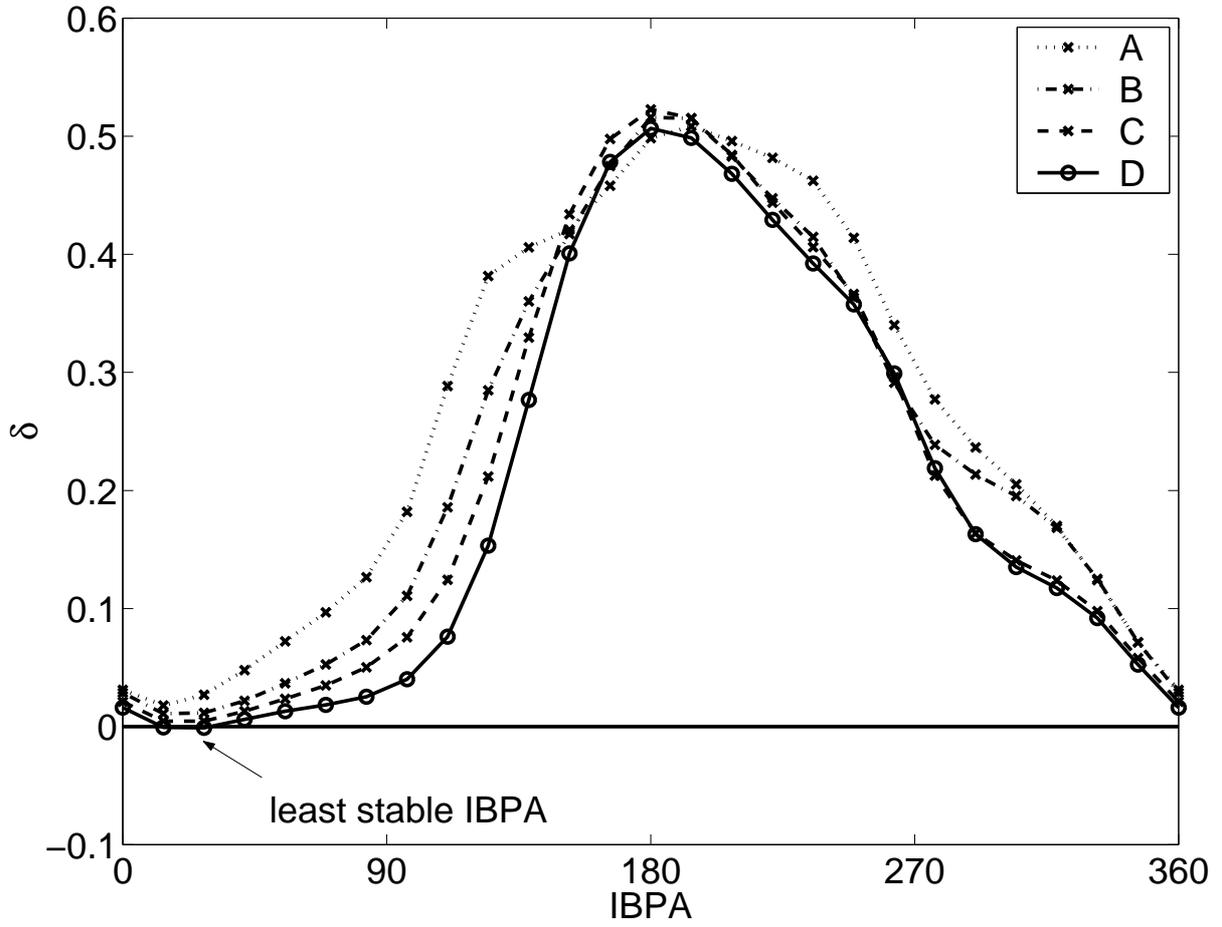
Figure 10: Flutter analysis of the 3D fan: logarithmic decrement for the 4 working conditions.

a)

b)
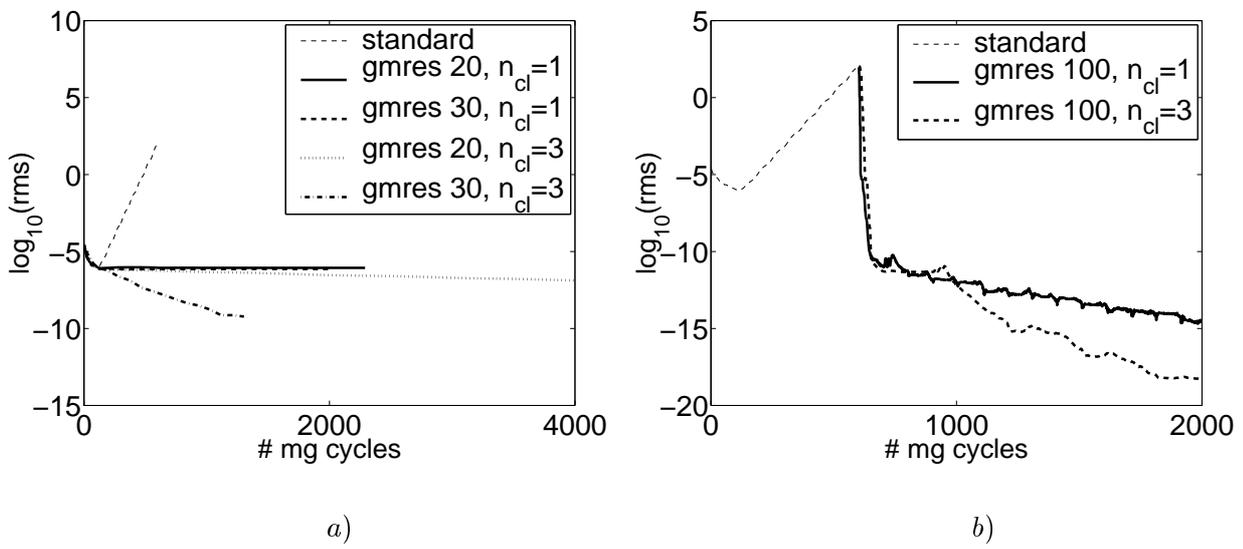
Figure 11: Flutter analysis of the 3D fan: convergence histories of *hydlin* for mean flow D and $IBPA = 180^o$.
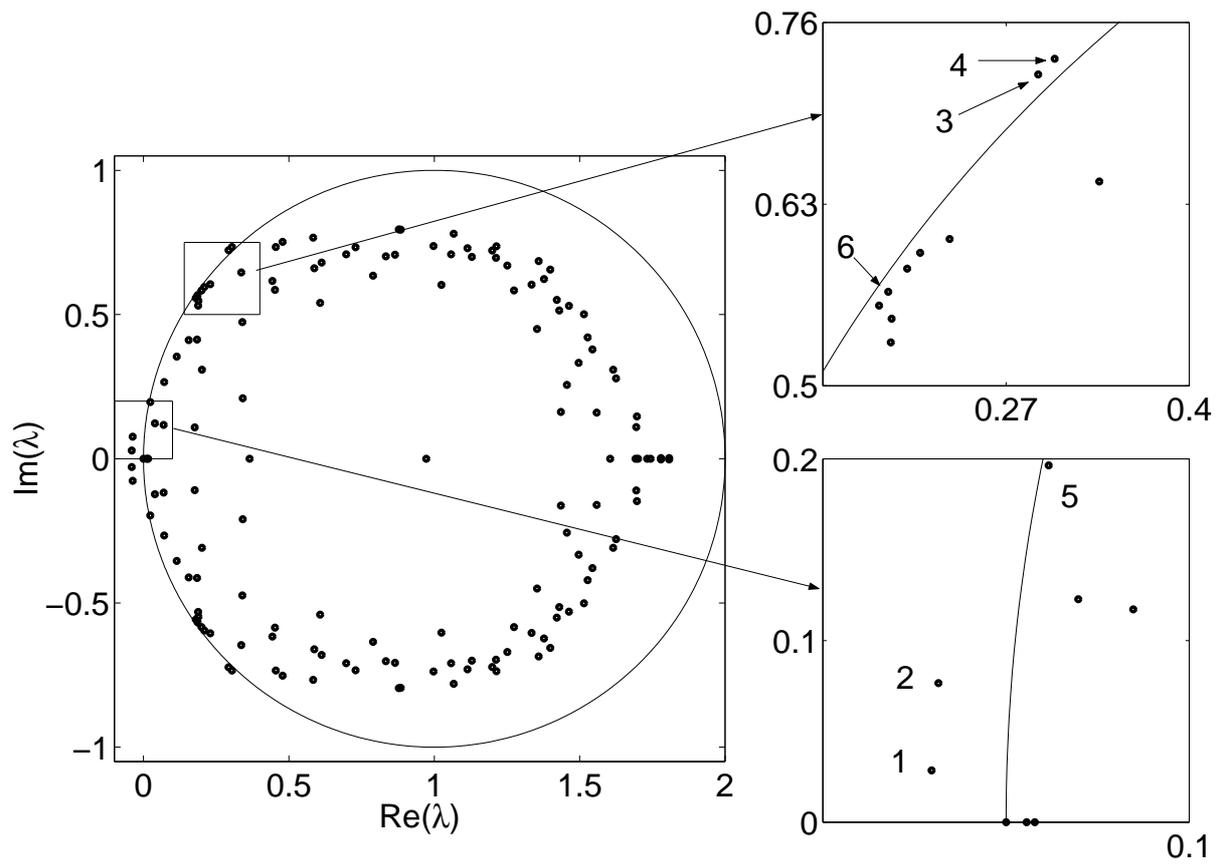
Figure 12: Flutter analysis of the 3D fan: first 150 dominant eigenvalues of $M^{-1}A$ ($n_{cl}\!=\!1$) for mean flow D and $IBPA\!=\!180^o$.
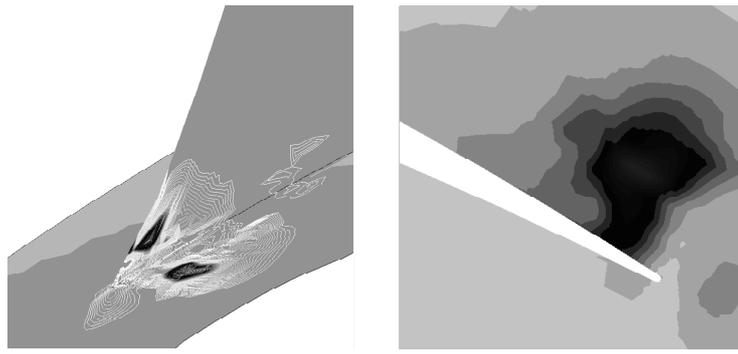
a)

b)
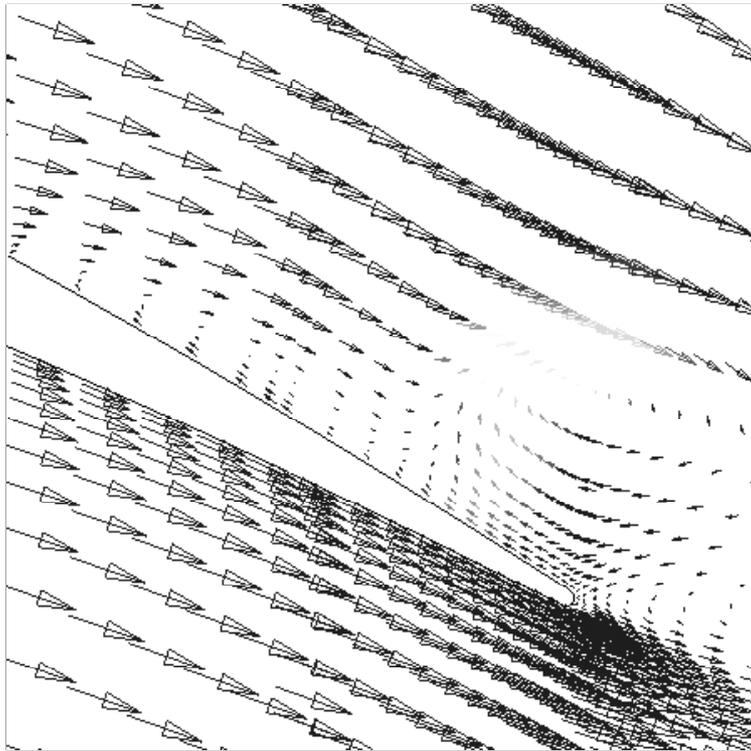
c)

Figure 13: Pressure amplitude of dominant eigenmode associated with the complex con-jugate pair 1: *a*) 3D view of the corner between the hub and the suction side close to the TE and *b*) blade-to-blade section close to the hub. *c*) Velocity vectors in blade-to-blade section close to the hub.